ChemComm

COMMUNICATION

View Article Online
View Journal | View Issue

Cite this: *Chem. Commun.*, 2025, **61**, 2317

Received 23rd September 2024,
Accepted 2nd January 2025

DOI: 10.1039/d4cc04927f

rsc.li/chemcomm

Alloying effect modulated electronic structure of Mo-doped PdIn bimetallene nanoribbons for ambient electrosynthesis of urea†

You Xu, Shiming Wang, Yueji Wu, Qiqi Mao,* Hongjie Yu, Kai Deng, Ziqiang Wang, Liang Wang * and Hongjing Wang *

Designing advanced catalysts for electrosynthesis of urea is of significance yet remains challenging. Herein, ultrathin two-dimensional Mo-doped PdIn bimetallene nanoribbons were synthesized *via* a one-pot method. Material characterization and electrochemical study revealed that the alloying effect enabled electron transfer from In to Pd and provided dual metal sites with regulated electronic structure for the adsorption and activation of NO_3^- and CO_2, thus facilitating the generation of key active intermediates and promoting the C–N coupling reaction.

The electrocatalytic coupling of CO_2 and nitrogen-containing molecules to generate urea stands as a promising alternative to achieve green urea synthesis.[1,2] Selecting suitable N-sources and designing efficient reaction systems are pressing needs for advancing the electrochemical synthesis of desired N-containing products.[3,4] Nitrate (NO_3^-) is considered to be a favorable N-source in the field of electrosynthesis of urea due to its higher solubility than N_2 in aqueous solution and relatively lower dissociation energy of the N=O bond (204 kJ mol^{-1}) than N≡N in N_2 (941 kJ mol^{-1}).[5,6] Additionally, in view of the fact that NO_3^- can come from wastewater, the electrochemical conversion of NO_3^- into value-added products can also potentially help to address the environmental issues resulting from NO_3^-.[7,8] An essential challenge for achieving considerable urea output *via* the C–N coupling of NO_3^- and CO_2 lies in its complex multi-step proton-coupled electron transfer processes, which is accompanied by the competing parallel electroreduction of CO_2/NO_3^- and the hydrogen evolution reaction (HER).[9] Therefore, to pursue high urea output, an ideal electrocatalyst for highly efficient C–N coupling should be capable of activating NO_3^- and CO_2 reactants, and reducing the probability of side reactions.[10]

In the field of electrocatalysis, palladium (Pd) has attracted widespread attention due to its excellent performance.[11] Pd-based nanomaterials exhibit high activity in both the carbon dioxide reduction reaction (CO_2RR) and nitrate reduction reaction (NO_3^-RR).[12] However, pure Pd cannot perform well for co-electroreduction of CO_2/NO_3^- to synthesize urea due to the monotonicity of the active site and poor tolerance of Pd to poisoning species.[13] Studies have shown that alloying Pd with other metals can effectively alter the electronic structure and optimize catalyst performance.[14,15] Notably, as a p-block metal, indium (In) exhibits a high hydrogen evolution overpotential, which can effectively suppress the HER and has been demonstrated to boost the CO_2RR and NO_3^-RR electrocatalysis.[16] Alloying Pd with In can not only regulate the electronic structure of Pd but also potentially bring about additional active sites, which is conducive to adsorption and coactivation of multiple reactants in the urea electrosynthesis reaction.[17] Proper control over the shape and structure of Pd-based catalysts can enable effective tuning of their properties for the desired applications.[18] With an abundance of active sites and considerable structural flexibility, 2D metallenes combine the benefits of 2D structures with the intrinsic properties of metals, which makes them more active and endows them with higher atomic utilization compared to other non-2D materials and their bulk equivalents.[19,20] Beyond frequently reported 2D metallene nanosheets or nanoplates, metallene nanoribbons featuring longitudinal extension of the metallene at the atomic level can simultaneously utilize the advantages of metallene and nanoribbons to boost the catalytic performance.[21] Based on the above analysis, Pd-based alloyed bimetallene nanoribbons hold promise as highly efficient catalysts for urea synthesis.

In this work, we synthesized atomically thin Mo-doped PdIn bimetallene nanoribbons (Mo–PdIn BNRs) by a one-pot method and employed them as electrocatalysts for the electrochemical synthesis of urea through the co-reduction of CO_2 and NO_3^- under ambient conditions. It was demonstrated that the alloying effect enables electron transfer from In to Pd and generates an electron-rich Pd site and electron-deficient In site. With the synergism of dual metal sites, the optimal urea yield rate over the Mo–PdIn BNRs reached 1016.49 μg h^{-1} mg_{cat}^{-1} with an FE of 18.42% at −0.4 V *vs.* RHE.

State Key Laboratory Breeding Base of Green-Chemical Synthesis Technology, College of Chemical Engineering, Zhejiang University of Technology, Hangzhou, Zhejiang 310014, P. R. China. E-mail: 1346326641@qq.com, wangliang@zjut.edu.cn, hjw@zjut.edu.cn

† Electronic supplementary information (ESI) available. See DOI: https://doi.org/10.1039/d4cc04927f

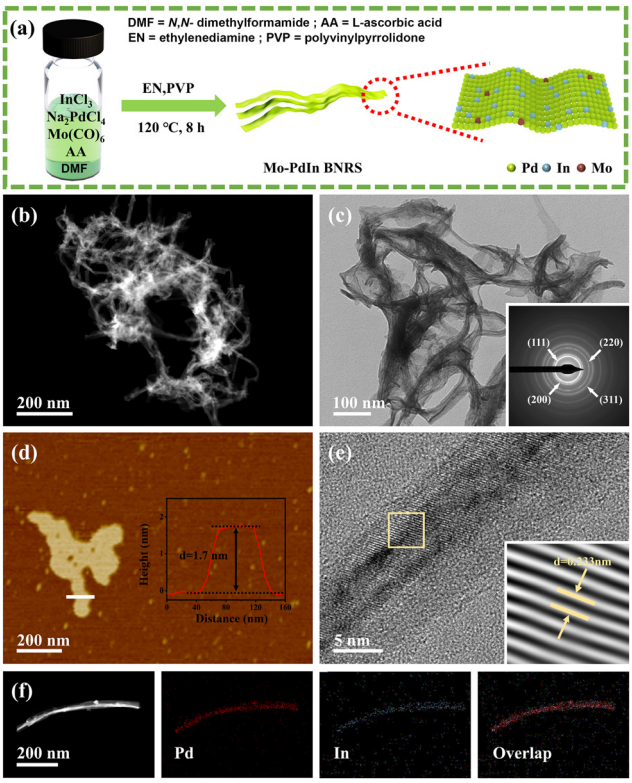

Fig. 1 (a) Schematic diagram of the synthetic process for Mo–PdIn BNRs. (b) HAADF-STEM image, (c) TEM image and SAED pattern, (d) AFM image and relevant height profile, (e) HRTEM image, (f) HAADF-STEM image and relevant EDX mappings of Mo–PdIn BNRs. The insets in (e) show the lattice fringes of the square region.

Fig. 1a shows the one-pot wet chemical method for synthesizing the Mo–PdIn BNRs, in which AA serves as the reducing agent, CO released from $Mo(CO)_6$ acts as a structural directing agent, and PVP and EN function as capping agents to ensure the longitudinal extension of metallene into nanoribbons.[22] As contrastive samples, Mo-doped Pd metallene nanoribbons (Mo–Pd MNRs) without In and PdIn bimetallene nanoribbons (PdIn BNRs) without Mo were also synthesized (Fig. S1–S4 and Table S1, ESI†). Transmission electron microscopy (TEM) and high-angle annular dark-field scanning TEM (HAADF-STEM) images reveal that Mo–PdIn BNRs possess an ultrathin nanoribbon morphology (Fig. 1b and c). Selected area electron diffraction (SAED) reveals clear concentric ring patterns (inset of Fig. 1c), indicating the polycrystalline nature of the Mo–PdIn BNRs. Atomic force microscopy (AFM) characterization further confirms the atomic thinness of Mo–PdIn BNRs, with a measured thickness of approximately 1.7 nm (Fig. 1d). This ultrathin two-dimensional nanostructure provides abundant active sites, which is beneficial to improving electrocatalytic performance. The high-resolution TEM (HRTEM) image shows lattice fringes with a spacing of 0.233 nm in the Mo–PdIn BNRs (Fig. 1e), corresponding to the (111) plane of the face-centered cubic (fcc) Pd-based alloy. HAADF-STEM and corresponding element mapping images demonstrate the uniform distribution of Pd and In elements in the bimetallene nanoribbons (Fig. 1f). Energy dispersive X-ray (EDX) spectrum and inductively coupled plasma optical emission spectroscopy (ICP-OES) further reveal the presence of trace amounts of Mo residue in the metallene nanoribbon, with an atomic ratio of Pd/In/Mo = 82.84/13.33/3.83 (Fig. S5 and Table S1, ESI†).

X-ray diffractometer (XRD) characterization was conducted to analyse the crystalline structure of the prepared samples. The XRD patterns of both Mo–PdIn BNRs and Mo–Pd MNRs show obvious diffraction peaks of the fcc structure of Pd (Fig. 2a). Specifically, compared to Mo–Pd MNRs without In introduction, the peak positions of Mo–PdIn BNRs show a shift to lower angle, indicative of the introduction of larger atomic radius In into the Pd crystal structure. In addition, X-ray photoelectron spectroscopy (XPS) was utilized to investigate the surface and electronic properties of the Mo–PdIn BNRs, Mo–Pd MNRs, and commercial In_2O_3 samples, with corresponding XPS survey spectra presented in Fig. 2b and Fig. S6 (ESI†). The high-resolution Pd 3d XPS spectrum shows that Pd in the bimetallene nanoribbons mainly exist in the metallic state (Fig. 2c), where the peaks located at 340.08 eV and 334.78 eV belong to Pd^0 $3d_{3/2}$ and $3d_{5/2}$ orbitals.[23] Compared to Mo–Pd MNRs, the binding energies of Pd^0 3d in Mo–PdIn BNRs exhibit a certain degree of negative shift, indicating the change in electronic configuration of Pd upon In introduction. As can be seen from the high-resolution In 3d XPS spectrum (Fig. 2d), there are two pairs of doublets including both a strong peak and a weak peak, where the more intense peaks are ascribed to the In in the oxidation state (*i.e.*, In^{3+}) and the weak peaks, with the binding energies lower than those of the In^{3+} oxidized states, are associated with the metallic In species. This suggested that the In was easily oxidized when exposed to air due to its oxophilic nature. Compared to pure In_2O_3 (see Fig. S7 for its SEM image, ESI†), the In^{3+} peak of Mo–PdIn BNRs has shifted significantly towards higher binding energy, possibly due to the strong influence of Pd. It can be inferred from the above results that strong electronic interaction exists between Pd and In through orbital hybridization upon alloying within the atomic level, which enables electron

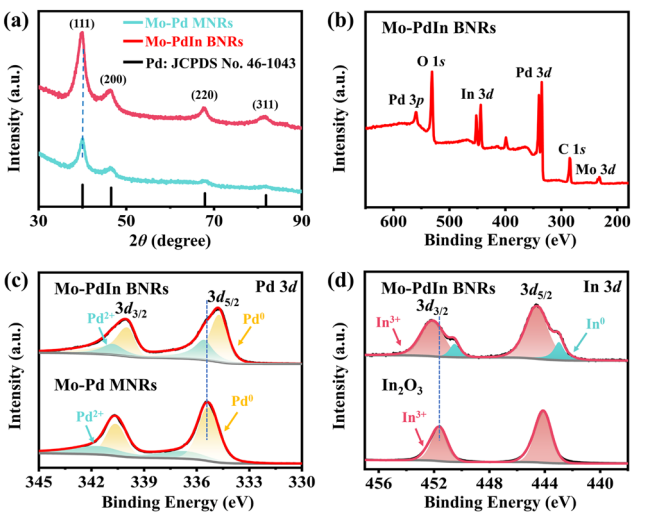

Fig. 2 (a) XRD patterns of Mo–PdIn BNRs and Mo–Pd MNRs. (b) XPS survey spectrum of the Mo–PdIn BNRs. (c) Pd 3d XPS spectra of Mo–PdIn BNRs and Mo–Pd MNRs. (d) In 3d XPS spectra of Mo–PdIn BNRs and In_2O_3.

transfer from In to Pd and generates an electron-rich Pd site and electron-deficient In site.

Under ambient conditions, the electrocatalytic performance of various catalysts for urea synthesis from CO_2 and NO_3^- was evaluated using an H-type electrolysis cell equipped with a typical three-electrode system (see ESI† for the details). Fig. 3a displays the linear sweep voltammetry (LSV) curves of Mo–PdIn BNRs measured in a 0.1 M KNO_3 solution saturated with Ar or CO_2. In the presence of CO_2 and NO_3^-, a significant increase in current density is observed, indicating a response of the catalyst to the co-reduction of CO_2 and NO_3^-. In a KNO_3 electrolyte solution saturated with CO_2, LSV curves reveal that the current density of the Mo–PdIn BNR catalyst is significantly higher than those of Mo–Pd MNRs and In_2O_3 (Fig. S8, ESI†), indicating a significant enhancement in electrocatalytic activity over Mo–PdIn BNRs due to their dual metal sites with regulated electronic structure.

Chronoamperometric (*i*–*t*) testing was performed at a potential range from −0.2 to −0.6 V *vs.* RHE for 2 h (Fig. S9, ESI†). The produced urea was quantitatively detected by the diacetylmonoxime method (Fig. S10, ESI†). NO_2^- and NH_3 were detected by ultraviolet-visible spectroscopy (UV-Vis) based on standard curves (Fig. S11 and S12, ESI†). Gas chromatography (GC) was employed to detect CO and H_2 gases. The urea FE and yield rate of Mo–PdIn BNRs, Mo–Pd MNRs and In_2O_3 at different potentials are shown in Fig. 3b and c. The testing results of Mo–PdIn BNRs exhibit a volcano shape, reaching a maximum yield of 1016.49 μg h^{-1} mg_{cat}^{-1} and a highest FE of 18.42% at −0.4 V *vs.* RHE. Obviously, the urea yield and FE of Mo–PdIn BNRs show significant enhancement compared to Mo–Pd MNRs and In_2O_3. Meanwhile, the PdIn BNRs without Mo exhibited similar urea electrosynthesis activity compared to the typical Mo–PdIn BNRs (Fig. S13, ESI†), indicating that the enhanced urea electrosynthesis capability over the Mo–PdIn BNRs mainly contributed to the synergistic effect of Pd and In dual metal sites. It is also worth noting that the typical Mo–PdIn BNR catalyst has a higher FE and urea yield compared with most reported electrocatalysts (Fig. S14 and Table S2, ESI†). The FE test results of urea, NO_2^-, NH_3, CO and H_2 at different potentials of Mo–PdIn BNRs are shown in Fig. S15 (ESI†). Comparison between Mo–Pd MNRs and In_2O_3 shows that FEs of the C-related products, which is mostly CO on Mo–Pd MNRs, are higher than those on In_2O_3 (Fig. S16, ESI†). Conversely, In_2O_3 obtains higher FEs of N-related products (*e.g.*, NO_2^-, NH_3) than Mo–Pd MNRs. These results might indicate that Pd and In are the active sites for CO_2 and NO_3^-, respectively. Moreover, compared with Mo–Pd MNRs, a sharp decrease in H_2 FE was observed on the Mo–PdIn BNRs, indicating the effective suppression of the competing HER reaction by the introduction of In. Obviously, Mo–PdIn BNRs exhibit higher urea FE and lower CO and NH_3 FEs relative to Mo–Pd MNRs, indicating that the related intermediates are more likely to be consumed for urea synthesis rather than converted into CO and NH_3. Furthermore, compared to other Mo–PdIn BNRs with a higher Pd content or a higher In content, the typical Mo–PdIn BNRs exhibit higher urea FE and lower CO and NH_3 FEs, while that with a higher In content shows a higher NH_3 FE, and that with a higher Pd content exhibits a higher CO FE (Fig. S17 and S18, ESI†), indicating that an excess of either Pd or In sites can lead to the further conversion of intermediates into CO or NH_3, rather than promoting C–N coupling for urea synthesis. The electrocatalytic stability of Mo–PdIn BNRs for urea synthesis was evaluated through 5 independent cycle testing. Negligible fluctuations in current density (Fig. S19, ESI†) were observed, and neither the urea yield nor the FE decreased significantly (Fig. 3d). Characterization by TEM (Fig. S20, ESI†), XRD (Fig. S21, ESI†) and XPS (Fig. S22, ESI†) for the post-tested Mo–PdIn BNRs demonstrates their morphological, compositional and crystal structure stability during the cycling testing.

The origin of N in urea synthesis was determined using ^{15}N isotope labelling. As shown in Fig. S23 (ESI†), $CO(^{15}NH_2)_2$ forms two main peaks at 5.42 and 5.56 ppm, and $CO(^{14}NH_2)_2$ has an obvious peak at 5.47 ppm. The ^1H nuclear magnetic resonance (NMR) spectrum confirms that the nitrogen of urea comes from NO_3^-RR. Comparison under different reaction conditions further shows that urea is produced by the electrocatalytic co-reduction of NO_3^- and CO_2 (Fig. S24, ESI†). In order to explore the reasons for the enhanced catalytic performance, the electrochemical properties of Mo–PdIn BNRs and Mo–Pd MNRs were further analyzed. Electrochemical impedance spectroscopy (EIS) shows that the Mo–PdIn BNRs have lower charge transfer resistance than both Mo–Pd MNRs and In_2O_3 (Fig. S25, ESI†), which is beneficial to accelerating the reaction kinetics. The double-layer capacitance (C_{dl}) measurement was applied to calculate the electrochemical surface area (ECSA) (Fig. S26, ESI†). The C_{dl} value of the Mo–PdIn BNRs is 1 mF cm^{-2}, which is higher than that of the Mo–Pd MNRs (0.6 mF cm^{-2}) and In_2O_3 (0.7 mF cm^{-2}) and indicates that the Mo–PdIn BNRs provide more accessible active sites.

To explore the mechanism of C–N coupling of CO_2 and NO_3^- to form urea, we further investigated the individual reduction capabilities of Mo–PdIn BNRs for CO_2 and NO_3^-. Ar was passed into 0.1 M KNO_3 solution to test the NO_3^-RR performance of the catalyst. CO_2 was passed into 0.1 M $KHCO_3$ solution to test the CO_2RR performance of the catalyst. As shown in Fig. S27 (ESI†), the FE of NH_3 for NO_3^-RR is much higher than that of co-reduction of NO_3^- and CO_2. In the absence of NO_3^-, the FE of CO also has the same increasing trend. This indicates that

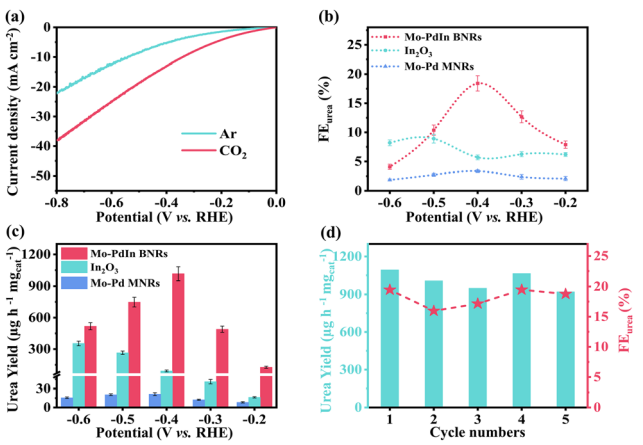

Fig. 3 (a) LSV curves of Mo–PdIn BNRs in a 0.1 M KNO_3 solution with Ar or CO_2 gas bubbling, respectively. (b) FE of urea and (c) urea yield of various catalysts at different applied potentials. (d) Urea yield and corresponding FEs of five independent cycles at −0.4 V *vs.* RHE, with each cycle of 2 h.

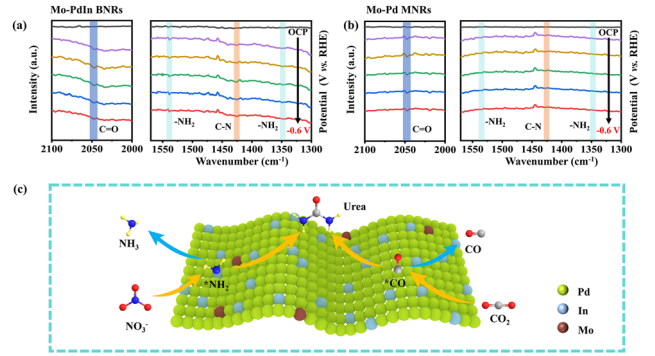

Fig. 4 *In situ* FTIR spectra of (a) Mo–PdIn BNRs and (b) Mo–Pd MNRs at various potentials. (c) The possible schematic diagram of urea synthesis over the Mo–PdIn BNRs.

C–N coupling occurs during the co-reduction process, resulting in a decrease in NH_3 and CO production.

To investigate the formation of key intermediates and role of the active sites, *in situ* Fourier transformed infrared spectroscopy (FTIR) was performed. As for Mo–PdIn BNRs (Fig. 4a), the infrared bands at 1540 and 1345 cm^{-1} are attributed to the stretching modes of $-NH_2$,[24,25] while those at 2047 cm^{-1} and 1425 cm^{-1} are assigned to the stretching of *CO and the stretching vibration of the C–N bond, respectively,[26] indicating that urea was electrochemically generated on the Mo–PdIn BNRs.[27] As shown in Fig. 4b, the C–N and $-NH_2$ bands on Mo–Pd MNRs exhibit significantly reduced intensities, suggesting that Mo–Pd MNRs have lower urea synthesis activity compared to Mo–PdIn BNRs. In contrast, the intensity of the *CO band on Mo–Pd MNRs is comparable to that on Mo–PdIn BNRs, indicating that Pd primarily catalyzes the $*CO_2 \rightarrow *CO$ reduction, leading to the formation of the key *CO intermediate. The weaker intensities of the C–N and $-NH_2$ on the Mo–Pd MNRs further highlight the critical role of In in promoting $*NH_2$ generation and facilitating the C–N coupling between *CO and $*NH_2$ to produce urea on the Mo–PdIn BNRs. Based on the above results, the reaction mechanism for electrochemical urea synthesis can be preliminarily inferred. The constructed Mo–PdIn BNRs could provide dual metal sites (*i.e.*, Pd and In) with regulated electronic structure for the adsorption and activation of NO_3^- and CO_2. During the reaction, NO_3^- is converted into $*NH_2$, CO_2 is converted into *CO, and urea is synthesized by C–N coupling of $*NH_2$/*CO intermediates on Mo–PdIn BNRs (Fig. 4c). Part of the $*NH_2$ and *CO continue to reduce to NH_3 and CO.

In summary, we successfully synthesized Mo–PdIn BNRs for electrochemical synthesis of urea under ambient conditions, reaching an optimal urea yield rate of 1016.49 $\mu g\ h^{-1}\ mg_{cat}^{-1}$ and an FE of 18.42%. It was demonstrated that the alloying effect could regulate the electronic structures of Pd and In and enable the creation of dual active sites for the adsorption and activation of NO_3^- and CO_2, thus facilitating the generation of key active intermediates and promoting the C–N coupling reaction to synthesize urea.

This research was supported National Natural Science Foundation of China under Grant No. 22278369, 22308330, 22372148, 22478345 and 22408333, and the Zhejiang Provincial Natural Science Foundation of China under Grant No. LR24B060001, LQ22B030012 and LQ23B030010.

Data availability

The data supporting this article have been included as part of the ESI.†

Conflicts of interest

There are no conflicts to declare.

Notes and references

1 C. Chen, S. Li, X. Zhu, S. Bo, K. Cheng, N. He, M. Qiu, C. Xie, D. Song, Y. Liu, W. Chen, Y. Li, Q. Liu, C. Li and S. Wang, *Carbon Energy*, 2023, **5**, 345.
2 Y. Kohlhaas, Y. S. Tschauder, W. Plischka, U. Simon, R.-A. Eichel, M. Wessling and R. Keller, *Joule*, 2024, **8**, 1579–1600.
3 Y. Li, S. Zheng, H. Liu, Q. Xiong, H. Yi, H. Yang, Z. Mei, Q. Zhao, Z. W. Yin, M. Huang, Y. Lin, W. Lai, S. X. Dou, F. Pan and S. Li, *Nat. Commun.*, 2024, **15**, 176.
4 Y. Wang, Y. Qin, W. Li, Y. Wang, L. Zhu, M. Zhao and Y. Yu, *Trans. Tianjin Univ.*, 2023, **29**, 275–283.
5 J. Leverett, T. Tran-Phu, J. A. Yuwono, P. Kumar, C. Kim, Q. Zhai, C. Han, J. Qu, J. Cairney, A. N. Simonov, R. K. Hocking, L. Dai, R. Daiyan and R. Amal, *Adv. Energy Mater.*, 2022, **12**, 2201500.
6 Y. Xu, H. Wang, T. Ren, H. Yu, K. Deng, Z. Wang, H. Wang and L. Wang, *Chem. Eng. J.*, 2024, **498**, 155557.
7 Y. Chen, A. Ma, L. Chen, X. Liu, Y. Li, Y. Hong, Y. Zhang, Y. Liu, L. Wei, Y. Li, S. Li and S. Liu, *Trans. Tianjin Univ.*, 2024, **30**, 488–497.
8 Y. Xu, Y. Wen, T. Ren, Z. Yu, H. Yu, K. Deng, Z. Wang, H. Wang and L. Wang, *Chem. Eng. J.*, 2024, **490**, 151519.
9 X. Zhang, X. Zhu, S. Bo, C. Chen, M. Qiu, X. Wei, N. He, C. Xie, W. Chen, J. Zheng, P. Chen, S. P. Jiang, Y. Li, Q. Liu and S. Wang, *Nat. Commun.*, 2022, **13**, 5337.
10 X. Huang, Y. Li, S. Xie, Q. Zhao, B. Zhang, Z. Zhang, H. Sheng and J. Zhao, *Angew. Chem., Int. Ed.*, 2024, **63**, e202403980.
11 G. Xing, D. Wei, H. Zhang, Z. Tian and J. Li, *Chin. J. Struct. Chem.*, 2023, **42**, 100021.
12 R. Yan, H. Yin, X. Zuo, W. Peng, X. Zhu, L. Shi, J. Hou, D. Wang, F. Ye, J. Li, B. Mao and C. Hu, *Appl. Catal., B*, 2025, **361**, 124609.
13 D. Bagchi, S. Sarkar, A. K. Singh, C. P. Vinod and S. C. Peter, *ACS Nano*, 2022, **16**, 6185–6196.
14 Z. Chen, F. Jing, M. Luo, X. Wu, H. Fu, S. Xiao, B. Yu, D. Chen, X. Xiong and Y. Jin, *Carbon Energy*, 2024, **6**, 443.
15 Y. Mun, S. Lee, A. Cho, S. Kim, J. W. Han and J. Lee, *Appl. Catal., B*, 2019, **246**, 82–88.
16 W. Ma, S. Xie, X. G. Zhang, F. Sun, J. Kang, Z. Jiang, Q. Zhang, D. Y. Wu and Y. Wang, *Nat. Commun.*, 2019, **10**, 892.
17 M. Xie, S. Tang, Z. Li, M. Wang, Z. Jin, P. Li, X. Zhan, H. Zhou and G. Yu, *J. Am. Chem. Soc.*, 2023, **145**, 13957–13967.
18 Y. Sheng, J. Xie, R. Yang, H. Yu, K. Deng, J. Wang, H. Wang, L. Wang and Y. Xu, *Angew. Chem., Int. Ed.*, 2024, **63**, e202410442.
19 B. Miao, W. Fang, B. Sun, F. Li, X. Wang, B. Xia and Y. Chen, *Chin. J. Struct. Chem.*, 2023, **42**, 100095.
20 M. Luo, Z. Zhao, Y. Zhang, Y. Sun, Y. Xing, F. Lv, Y. Yang, X. Zhang, S. Hwang, Y. Qin, J. Y. Ma, F. Lin, D. Su, G. Lu and S. Guo, *Nature*, 2019, **574**, 81–85.
21 S. Liu, H. Zhang, H. Yu, K. Deng, Z. Wang, Y. Xu, L. Wang and H. Wang, *Appl. Catal., B*, 2023, **336**, 122948.
22 B. Ni, Q. Zhang, C. Ouyang, S. Zhang, B. Yu, J. Zhuang, L. Gu and X. Wang, *CCS Chem.*, 2020, **2**, 642–654.
23 H. Yu, T. Zhou, Z. Wang, Y. Xu, X. Li, L. Wang and H. Wang, *Angew. Chem., Int. Ed.*, 2021, **60**, 12027–12031.
24 J. Jiang, G. Wu, M. Sun, Y. Liu, Y. Yang, A. Du, L. Dai, X. Mao and Q. Qin, *ACS Nano*, 2024, **18**, 13745–13754.
25 X. F. Qiu, J. R. Huang, C. Yu, X. M. Chen and P. Q. Liao, *Angew. Chem., Int. Ed.*, 2024, **63**, e202410625.
26 Y. Zhang, Z. Li, K. Chen, X. Yang, H. Zhang, X. Liu and K. Chu, *Adv. Energy Mater.*, 2024, **14**, 2402309.
27 Y. Zhang, Z. Li, C. Qiang, K. Chen, Y. Guo and K. Chu, *ACS Nano*, 2024, **18**, 25316–25324.

